

VIP Very Important Paper

www.batteries-supercaps.org

Tailoring the Composition of Ternary NiCoFe Layered Double Hydroxide with Graphitic Carbon Nitride as a Positive Electrode Material for High-Performance Hybrid Supercapacitors

Elaiyappillai Elanthamilan^[a] and Sea-Fue Wang^{*[a]}

This work reports a simple hydrothermal-assisted method to prepare a high-performance nickel cobalt iron layered double hydroxide/graphitic carbon nitride ($\text{NiCoFe LDH/g-C}_3\text{N}_4$) composite for supercapacitor (SC) applications. Various spectral and analytical techniques were used to confirm the formation of $\text{NiCoFe LDH/g-C}_3\text{N}_4$ composite. The $\text{NiCoFe LDH/g-C}_3\text{N}_4$ composite demonstrates battery-like SC behavior in the three-electrode measurements. The $\text{NiCoFe LDH/g-C}_3\text{N}_4$ composite has a maximum specific capacity (366 C g^{-1} at 1 A g^{-1}) compared to the individual NiCoFe LDH and $\text{g-C}_3\text{N}_4$ electrode materials. Further, the $\text{NiCoFe LDH/g-C}_3\text{N}_4$ composite electrode shows 89% capacity retention even after 8000 galvanostatic

charge-discharge (GCD) cycles at 6 A g^{-1} . In addition, a hybrid supercapacitor (HSC) is fabricated by using $\text{NiCoFe LDH/g-C}_3\text{N}_4$ composite as a positive electrode and activated carbon (AC) as a negative electrode. The as-fabricated $\text{NiCoFe LDH/g-C}_3\text{N}_4/\text{AC}$ HSC demonstrates an impressive energy density of 76.44 Wh kg^{-1} and a power density of 1279.9 W kg^{-1} , along with excellent long-term cycle stability of 83% capacity retention even after 6000 GCD cycles at 6 A g^{-1} . Considering its simplicity of fabrication and exceptional energy storage capabilities, the as-fabricated $\text{NiCoFe LDH/g-C}_3\text{N}_4/\text{AC}$ hybrid supercapacitor has significant promise for practical use in the near future.

Introduction

Indisputably, energy is one of the world's primary concerns in the 21st century. New energy conversion and storage technologies that are efficient, affordable, and kind to the environment are urgently needed to address both the demands of contemporary civilization and the growing number of environmental issues.^[1] At present, supercapacitors (SCs) and fuel cells are both crucial for the efficient storage and conversion of electrochemical energy, playing a significant role in sustainable energy solutions.^[2]

SCs are the perfect choice because of their sufficient power density and extended cycle life. Furthermore, SCs can utilize the benefits of both conventional capacitors and rechargeable batteries, compensating for the shortcomings accompanying both.^[3] Nevertheless, the practical utilization of supercapacitors is limited due to their low energy density. Over time, researchers have focused on developing high-performance electrode materials to overcome this problem, using the energy density calculation method $E = 1/2 CV^2$.^[4] Many recent studies consistently demonstrated that transition metal oxides (TMOs) and their hydroxides, conductive polymers, and carbon-based electrode materials are the predominant choices for electrode

materials.^[5] Recently, Puritut Nakhanivej et al.^[6] prepared a free-standing oxidized black phosphorus with reduced graphene oxide for supercapacitor applications. The oxidized black phosphorous-based electrode shows a specific capacitance of 478 F g^{-1} at 1 A g^{-1} with 91% capacitance retention in over 50,000 galvanostatic charge-discharge (GCD) cycles. Qingyong Wang et al.^[7] prepared a cobalt/nickel boride/sulfide (Co-Ni-B-S) electrode material, which exhibited the specific capacitance of 1281 F g^{-1} at 1 A g^{-1} in the SC applications. Further, Co-Ni-B-S based SC device exhibit a high energy density of 50.0 Wh kg^{-1} at a power density of 857.7 W kg^{-1} .

Among transition metals-based hydroxides, the hydroxide-like structured layered double hydroxide (LDH) has gained significant interest in scientific curiosity. The LDH composition is represented by the acronym $[\text{M}^{2+}]_{1-x}[\text{M}^{3+}]_x(\text{OH})_{2x-y}(\text{H}_2\text{O})_y$; in which, An^- stands for anions; M^{2+} stands for divalent cations; and M^{3+} for trivalent cations.^[3a,8] Extensive research has consistently demonstrated the numerous advantages of LDH, such as the layers of LDH promoting fast ion diffusion, abundant active sites, and improved surface area.^[9] The layer of LDH comprises different metal cations with adjustable valence, allowing for a wide range of valence states that can enhance the capacity.^[3a,9] Further, previous reports have extensively examined the remarkable anion exchangeability of LDH. The incorporation of different types of anions effectively controls the distance between the layers. The increased distance between the layers minimizes the resistance and enhances the rate of ions diffusions.^[10] The LDH interlayer can experience synergistic effects because of the presence of multiple metal ions, thereby enhancing the specific capacity and cycle performance.^[11]

[a] E. Elanthamilan, S.-F. Wang

Department of Materials and Mineral Resources Engineering, National Taipei University of Technology, No. 1, Sec. 3, Chung-Hsiao East Rd., Taipei 106, Taiwan
E-mail: sfwang@ntut.edu.tw

 Supporting information for this article is available on the WWW under
<https://doi.org/10.1002/batt.202400754>

Based on the previous reports, the electrochemical properties of the ternary NiCoFe LDH, which contains both nickel and cobalt, were found to be superior compared to the binary NiFe LDHs or CoFe LDHs.^[12] Currently, it is possible to incorporate two and three or four metallic ions into the layers of LDH, forming a unified material. Further, the ternary/quaternary LDH possess a range of metal ions and often exhibit impressive supercapacitor behaviors, owing to its abundant active species, diverse structures, and improved capacity.^[13]

Hence, NiCoFe LDH is a promising material for energy storage devices, owing to its unique structure, which consists of three different metal ions with redox properties, and its 2D interlayer nature that provides a vast interlayer space. These characteristics of NiCoFe LDH enhance the ion and electron transfer, making it highly effective in improving energy storage ability.^[14] However, the primary disadvantage of hydroxides and LDHs is their low chemical stability, resulting in a restricted cycle life. Many methods can be employed to overcome these drawbacks. For instance, composites may be produced by utilizing electrochemically resistant materials like TMOs and carbonaceous materials.^[15]

Graphitic carbon nitride ($\text{g-C}_3\text{N}_4$) is a nitrogen heteroatom-substituted graphite framework. It possesses a two-dimensional structure that is remarkably flat, with a notably high surface area. Typically, $\text{g-C}_3\text{N}_4$ is known for being a highly crystallized polymer that exhibits rapid charge transfer in one direction. It has garnered significant attention from researchers because it can minimize interfacial impedance, simple synthesis procedures, and stability. With its high nitrogen content, $\text{g-C}_3\text{N}_4$ enhances the electrochemical properties of pseudocapacitors. Additionally, it exhibits excellent electron-donor properties, surface polarity, and electric conductivity.^[16]

Scientists categorize supercapacitors into three groups, symmetric, asymmetric, and hybrid, based on their structures, which improve the energy density and expand an active set potential window. The symmetric (same materials) and asymmetric (different materials) supercapacitors are made with positive and negative electrodes, typically a combination of EDLC and pseudocapacitor materials. However, the hybrid supercapacitor consists of battery-type material as the positive electrode and EDLC type as the negative electrode. By utilizing those electrodes made of different materials, the potential window for operation can be expanded, resulting in a significant improvement in both supercapacitor performance and energy density.^[17]

In the present study, the NiCoFe LDH/ $\text{g-C}_3\text{N}_4$ composite was prepared using the hydrothermal method and used for supercapacitor application. As a result, the NiCoFe LDH/ $\text{g-C}_3\text{N}_4$ composite electrode shows an impressive specific capacity of 366 C g^{-1} at 1 A g^{-1} in a three-electrode system. Further, NiCoFe LDH/ $\text{g-C}_3\text{N}_4$ composite shows excellent cycle stability. The as-constructed NiCoFe LDH/ $\text{g-C}_3\text{N}_4$ //AC HSC exhibits a high energy density of 76.44 Wh kg^{-1} at a power density of 1279.9 W kg^{-1} . These results proved that the NiCoFe LDH/ $\text{g-C}_3\text{N}_4$ //AC HSC performs satisfactorily in energy storage applications, with high energy densities and power densities and long-term cyclic stability.

Experimental Methods

Chemicals and Characterization techniques

The chemicals used and the characterization details were given in the supporting information.

Preparation of NiCoFe LDH

A simple hydrothermal method was used to synthesize the NiCoFe LDH. A range of 0.1 M solutions, including $\text{Ni}(\text{NO}_3)_2 \cdot 6\text{H}_2\text{O}$, $\text{Co}(\text{NO}_3)_2 \cdot 6\text{H}_2\text{O}$, and $\text{Fe}(\text{NO}_3)_3 \cdot 9\text{H}_2\text{O}$ were combined with a consistent quantity of $\text{CO}(\text{NH}_2)_2$ (0.5 M) in 70 ml of DI water. Afterward, the mixture was stirred using a magnetic stirrer until all the precursors dissolved completely. It was then transferred to an autoclave and kept at 120°C for 10 h. Then, the precipitate was collected and washed using a water-ethanol mixture and dried at 60°C . The resultant product was designated as NiCoFe LDH.

Preparation $\text{g-C}_3\text{N}_4$

The $\text{g-C}_3\text{N}_4$ was prepared using the thermal polymerization technique. A quantity of 3 g of melamine ($\text{C}_3\text{N}_3(\text{NH}_2)_3$) was placed in a boat crucible and subjected to heating in a tubular furnace at 600°C for 3 h in an inert atmosphere. The material was allowed to reach the ambient temperature after the heat treatment. The obtained yellowish bulk powder was washed and dried at 80°C to get pure $\text{g-C}_3\text{N}_4$.

Preparation of NiCoFe LDH/ $\text{g-C}_3\text{N}_4$ Composite

In this typical synthesis procedure, a range of 0.1 M solutions, including $\text{Ni}(\text{NO}_3)_2 \cdot 6\text{H}_2\text{O}$, $\text{Co}(\text{NO}_3)_2 \cdot 6\text{H}_2\text{O}$, and $\text{Fe}(\text{NO}_3)_3 \cdot 9\text{H}_2\text{O}$ were mixed with a consistent quantity of $\text{CO}(\text{NH}_2)_2$ (0.5 M) in 70 ml of DI water. Then, 50 mg of the as-prepared $\text{g-C}_3\text{N}_4$ was dispersed into the reaction mixture. Afterward, the solution was stirred using a magnetic stirrer until all the precursors dissolved completely. It was then transferred to an autoclave and kept at 120°C for 10 h. Then, the precipitate was collected and washed using a water-ethanol mixture and dried at 60°C . The resultant product was designated as NiCoFe LDH/ $\text{g-C}_3\text{N}_4$. Figure 1 shows the schematic representation of the synthesis of NiCoFe LDH/ $\text{g-C}_3\text{N}_4$ composite.

Electrode Fabrication

The details of the electrode fabrication, supercapacitor measurements, and corresponding equations are given in the supporting information.

Results and Discussion

Structural, Chemical and Morphological Analysis

The XRD analysis of the as-prepared samples is given in Figure 2A. From Figure 2A, it is clear that all the peaks in NiCoFe LDH correspond to $\text{Ni}_6\text{Fe}_2\text{CO}_3(\text{OH})_{16} \cdot 3\text{H}_2\text{O}$ (JCPDS card no. 40-0215) with the rhombohedral crystal system and space group of R. The peaks of NiCoFe LDH can be observed at various angles, indicating the presence of different crystal planes. These angles include 11.7° , 23.5° , 34.4° , 38.8° , 46.5° , 59.3° , and 60.8° , corresponding to the crystal planes (003), (006), (101), (015),

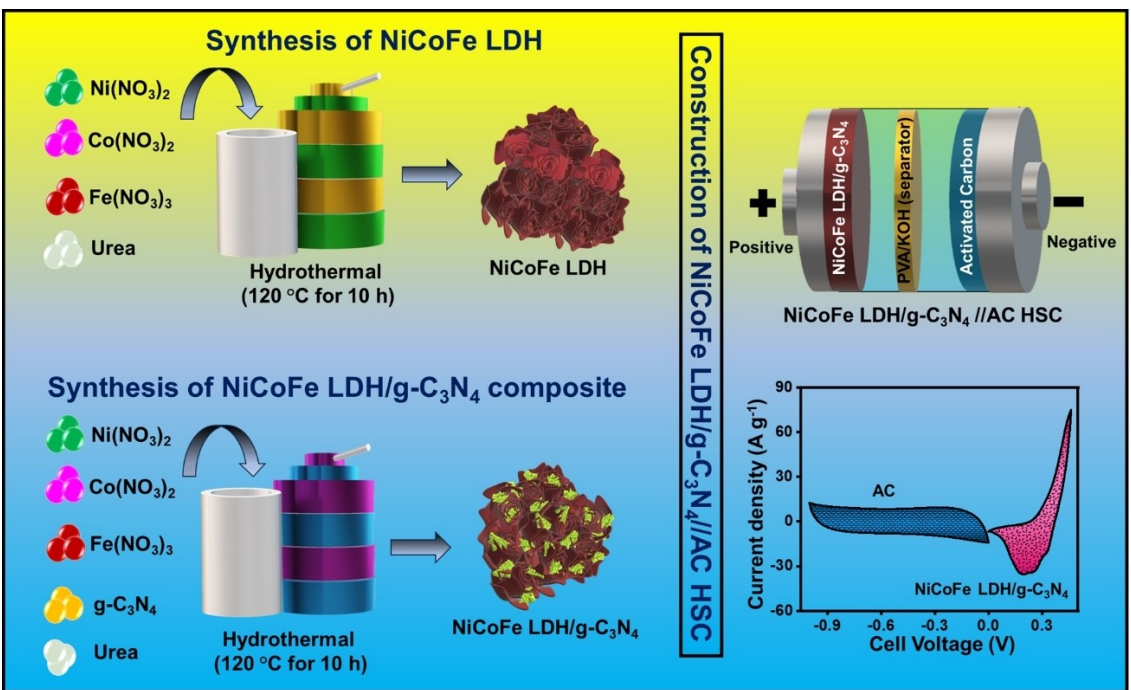


Figure 1. Schematic representation of the synthesis of NiCoFe LDH/g-C₃N₄ composite for hybrid supercapacitor applications

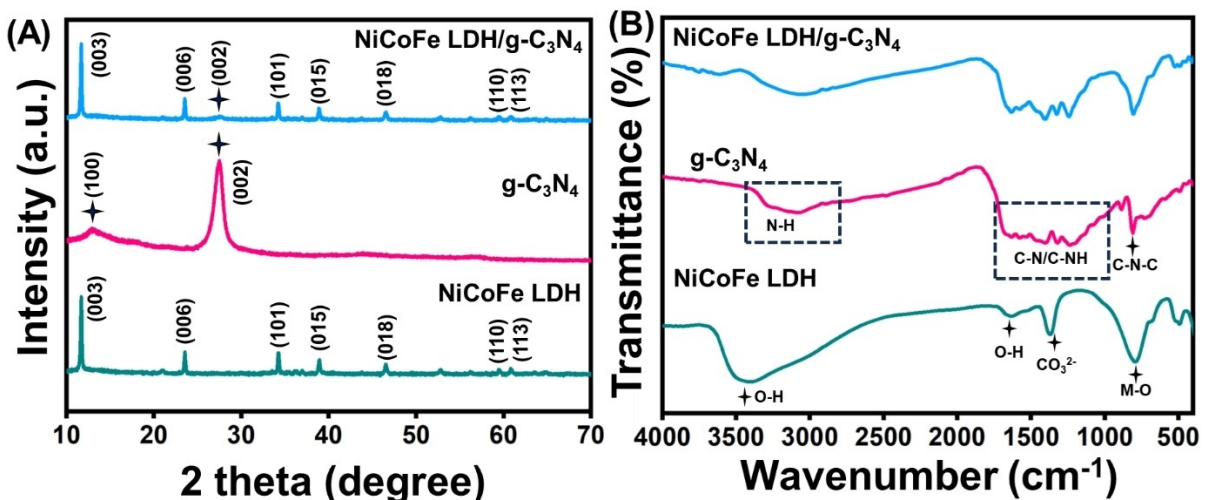


Figure 2. (A) XRD and (B) FTIR spectrum of NiCoFe LDH, g-C₃N₄, and NiCoFe LDH/g-C₃N₄ composite

(018), (110), and (113), respectively.^[18] Additionally, the distinct peaks of g-C₃N₄ are observed at 13.1° and 27.5°, corresponding to the crystal planes (100) and (002).^[19] The XRD pattern of the NiCoFe LDH/g-C₃N₄ composite shows all the characteristic peaks of NiCoFe LDH and g-C₃N₄, suggesting that the formation of the composite was successful and no additional impurities were present. Furthermore, the average crystallite size of the samples was calculated from the Debye-Scherrer equation (eqn. 1).^[20] The results showed that the average crystallite size for NiCoFe LDH was ~57 nm, while for the NiCoFe LDH/g-C₃N₄ composite, it was ~62 nm.

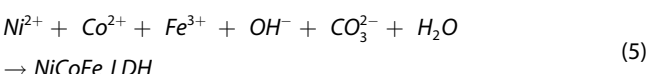
$$D = \frac{K\lambda}{\beta \cos\theta} \quad (1)$$

Figure 2B displays the FT-IR spectrum of the as-prepared samples. From the FT-IR spectrum of NiFeCo LDH, it is observed that there are four distinct peaks at 3416 cm⁻¹, 1636 cm⁻¹, 1378 cm⁻¹, and 750 cm⁻¹, which can be attributed to different vibrations, such as the stretching vibration of O—H, the hydrogen bonding of the hydroxide OH group, the vibration of CO₃²⁻ in the interlayer of LDH, and the stretching mode of Metal—Oxygen bond.^[3a,21] In the FTIR spectrum, a broad peak was observed at 1200–1600 cm⁻¹, indicating the presence of CN

heterocycles. Additionally, a broad peak at 3000–3500 cm⁻¹ suggested the presence of O–H bands and N–H components. Another peak at 810 cm⁻¹ indicated the presence of the triazine ring in the g-C₃N₄ systems.^[14,19a] The NiFeCo LDH/g-C₃N₄ composite exhibits characteristic peaks from both NiFeCo LDH and g-C₃N₄, indicating the successful formation of the composite.

In addition, Figure S1 illustrates the Raman spectra of NiCoFe LDH, g-C₃N₄, and the NiCoFe LDH/g-C₃N₄ composite. The Raman spectra of NiCoFe LDH possess three peaks at 455 cm⁻¹, 490 cm⁻¹, and 530 cm⁻¹, attributed to the vibrational modes of Ni–O, Co–O O, and Fe–O O, respectively.^[22] The Raman spectra of g-C₃N₄ exhibit a peak at 745 cm⁻¹, corresponding to the heptazine ring's vibrations. The signal at 1398 cm⁻¹ is attributed to sp³ carbon molecules resulting from surface imperfections. This peak may be attributed to the D band of g-C₃N₄. The signal at 1555 cm⁻¹ belongs to the G band of g-C₃N₄, obtained from sp² carbon atoms.^[23] The Raman peaks of the NiCoFe LDH/g-C₃N₄ composite exhibited the peaks

characteristic peaks of both NiCoFe LDH and NiCoFe LDH/g-C₃N₄ composite. In addition, the plausible synthesis mechanism of NiCoFe LDH is given in Equation. (2–5)^[24]



The morphology of the samples, including NiCoFe LDH, g-C₃N₄, and NiCoFe LDH/g-C₃N₄, was examined using SEM. The SEM images in Figure 3(A and B) show the synthesized NiCoFe LDH with a unique flower-like shape composed of assembled nanosheets. Figure 3(C and D) shows the morphology of g-C₃N₄, which consists of irregular enfolded and crumpled flake-like

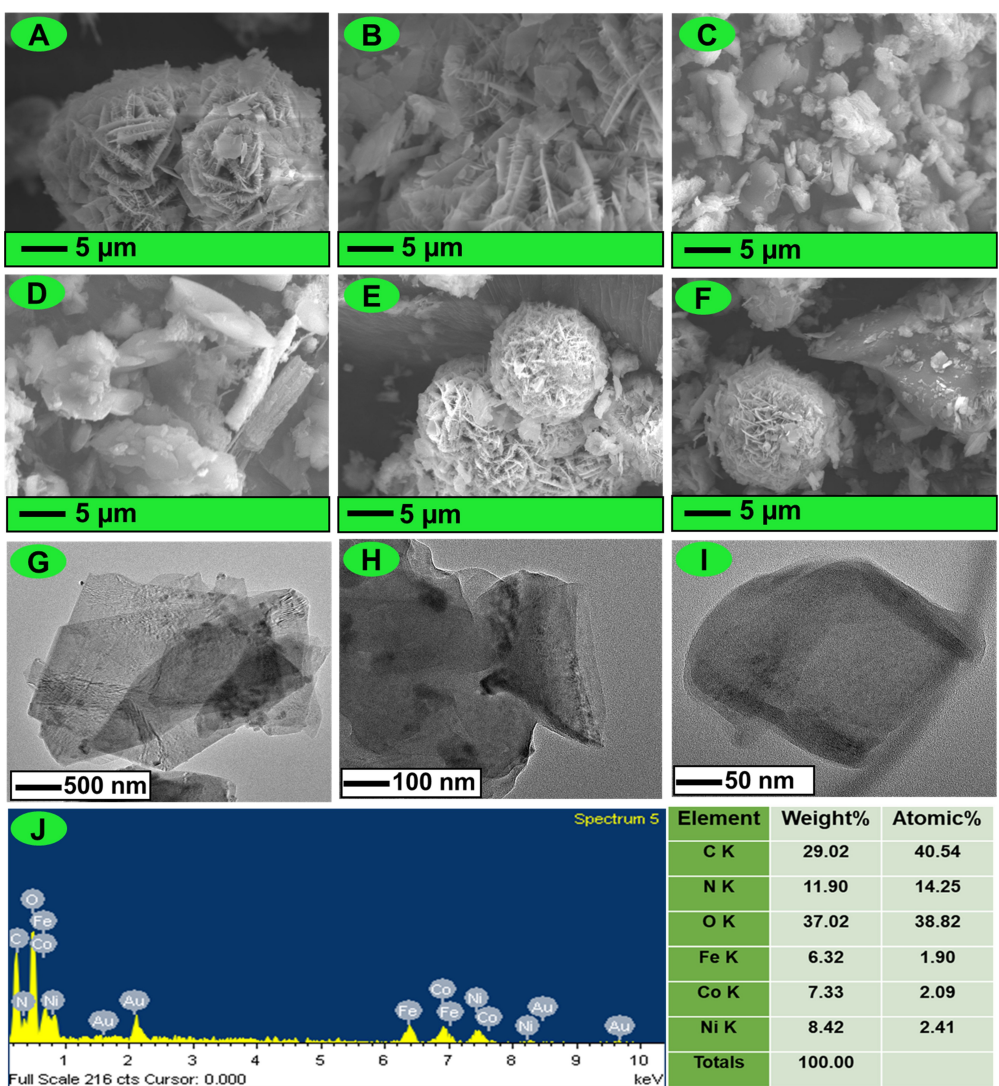


Figure 3. SEM images of (A and B) NiCoFe LDH (C and D) g-C₃N₄ (E and F) NiCoFe LDH/g-C₃N₄ composite (G–I) TEM images of NiCoFe LDH/g-C₃N₄ composite (J) EDAX analysis of NiCoFe LDH/g-C₃N₄ composite

structures. In addition, the SEM images of the NiCoFe LDH/g-C₃N₄ composite (Figure 3 (E and F)) reveal the preserved flower-like structure of the LDHs and the retained morphology of the g-C₃N₄ nanoflakes following the formation of the composite. The TEM analysis (Figure 3(G-I)) analysis shows the layer like morphology of of NiCoFe LDH embedded with g-C₃N₄. In addition, NiCoFe LDH nanoflowers' formation is prevented when combined with g-C₃N₄ to create a composite. By combining the morphological features of NiCoFe LDH (nanosheets) and g-C₃N₄ (nanoflake), the insertion of multiple electrolyte ions can be enhanced, resulting in a substantial increase in the surface area of the composite. As a result, the specific capacity of the electrode materials is significantly improved.^[14,17c]

To investigate the composition of the NiCoFe LDH/g-C₃N₄ composite, the elemental constituents and their spatial distributions were determined using energy dispersive X-ray (EDAX) measurements (Figure 3J) and elemental color mapping analysis (Figure S2(A-G)). According to Figure 3J, NiCoFe LDH/g-C₃N₄ comprises Ni, Co, Fe, C, and N. These elements are evenly distributed throughout the samples. It has been noted that

when component components have a homogeneous distribution, the NiCoFe LDH and g-C₃N₄ phases are intimately connected and thoroughly mixed within the NiCoFe LDH/g-C₃N₄ composite rather than existing as distinct aggregations in the composite.

An XPS analysis was implemented to assess the elemental composition and valence information samples. The Ni, Co, Fe, O, C, and N elements are composed in NiCoFe LDH/g-C₃N₄ composite as indicated by the overall survey spectrum (Figure 4A). As shown in Figure 4B, the two spin-orbit double peaks show as Ni 2p spectrum at 854.0 and 871.0 eV corresponds to Ni2p_{3/2} and Ni 2p_{1/2}. In brief, it was fitted into four peaks at 854.2, 855.2, 871.5 and 873.3 eV for Ni²⁺ and Ni³⁺ states, respectively. The two satellite peaks were noted at 860.9 eV and 879.4 eV.^[25] The Co 2p spectrum (Figure 4C) shows two spin-orbit double peaks at the binding energies of 779.0 and 795.0 eV, respectively, for Co 2p_{3/2} and Co 2p_{1/2}. The co-existence of Co²⁺ and Co³⁺ in Co 2p_{3/2} are fitted at 778.8 and 780.5 eV. The co-existence of Co²⁺ and Co³⁺ in Co 2p_{1/2} are fitted at 795.1 eV and 796.5 eV. The satellite peaks of Co 2p at 786.1 and 802.4 eV.^[26] The XPS spectrum of Fe 2p (Figure 4D)

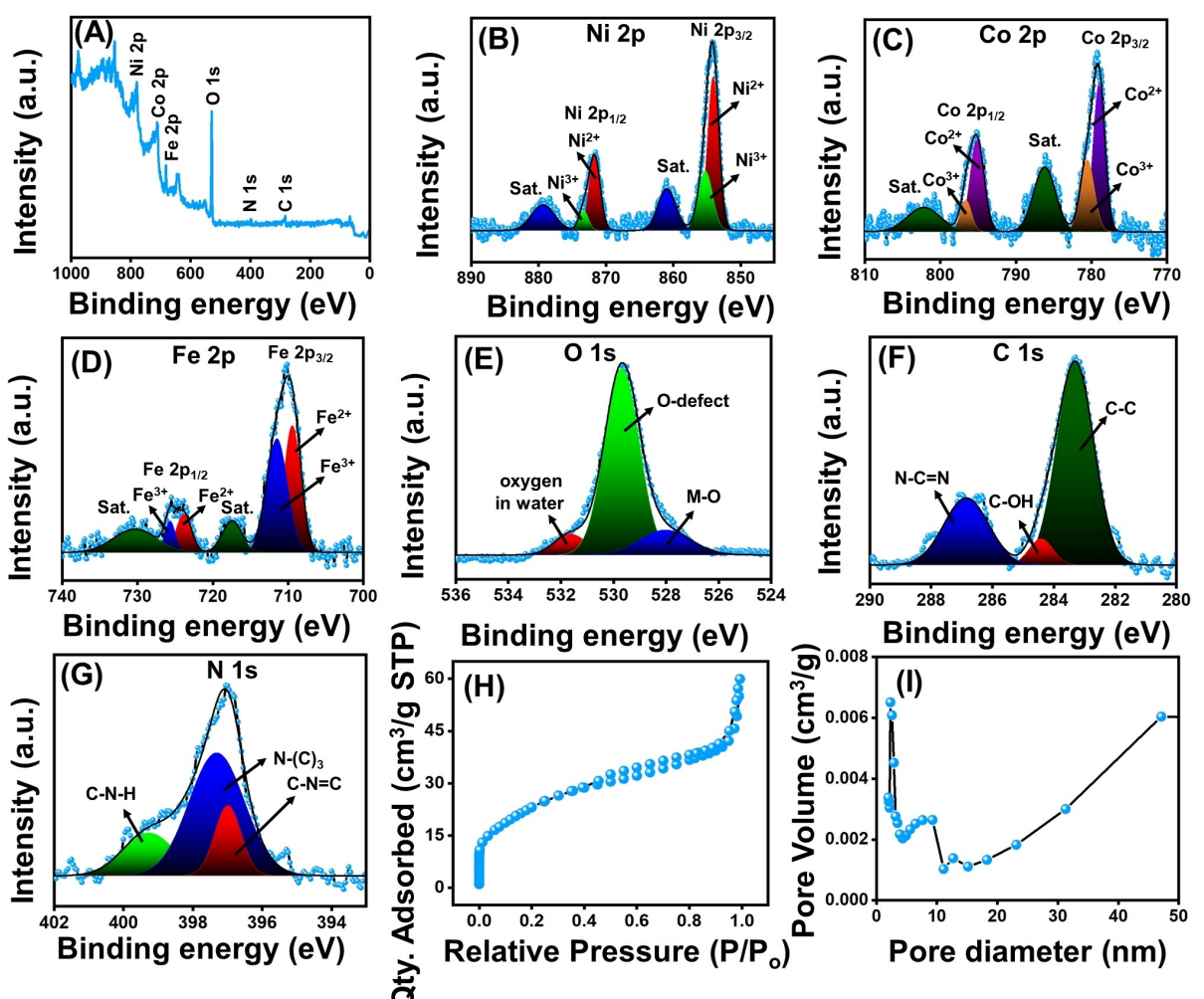


Figure 4. (A) XPS survey spectrum and high-resolution spectrum of (B) Ni 2p (C) Co 2p (D) Fe 2p (E) O 1s (F) C 1s and (G) N 1s spectrum of NiCoFe LDH/g-C₃N₄ composite (H) N₂ adsorption-desorption curve and (I) Pore size distribution curve of NiCoFe LDH/g-C₃N₄ composite

Fe 2p_{3/2} and Fe 2p_{1/2} shows the two spin-orbit double peaks at 709.9 and 724.8 eV, respectively. The fitted peaks at 709.5 eV and 723.7 eV correspond to Fe²⁺ states, and those at 711.4 and 725.7 eV correspond to Fe³⁺ states.

The satellite peaks of Fe 2p are noted at 717.5 and 730.4 eV.^[3a] Further, the O 1s spectrum (Figure 4E) shows three peaks at 528.0, 529.6, and 531.6 eV related to the metal-oxygen bonds, the defects in oxygen and the adsorbed water molecules on the surface of the sample. The C 1s spectrum can be resolved into three distinct peaks located at about 283.3, 284.4, and 286.8 eV (Figure 4F). These peaks correspond to the C-C (sp^2) bond, C-OH bond, and sp^2 N-C=N bond in the triazine units of g-C₃N₄, respectively. The N 1s XPS signals can be deconvoluted into three distinct peaks with binding energies of 396.9 eV, 397.3 eV, and 400.0 eV. These peaks correspond to the presence of C-N-C groups, N-(C)₃ groups, and C-N-H bonds, respectively (Figure 4G).^[19a] The results indicate that the NiCoFe LDH/g-C₃N₄ composite has been successfully formed and exhibits a diverse distribution of valence states, which is advantageous for enhancing electrochemical performance.^[17c,d]

The NiCoFe LDH/g-C₃N₄ composite materials were subjected to N₂ adsorption-desorption isotherm analysis to determine specific surface area and pore size distribution using Brunauer-Emmett-Teller (BET) and Barrett-Joyner-Halenda (BJH) methods. The NiCoFe LDH/g-C₃N₄ composite shows a type-IV isotherm curve with an H4 hysteresis loop illustrated in Figure 4H. The average pore volume, pore diameter, and BET surface area of the NiCoFe LDH/g-C₃N₄ composite were determined to be 3.36 nm, 0.07 cm³ g⁻¹, and 80.2955 m² g⁻¹, respectively. The results obtained from the BET measurement were also corroborated by the pore size distribution curve (PSD) (Figure 4I). The electrochemical performance was subsequently enhanced by the substantially increased SSA of the composite and porosity, which exposed more redox active sites for ion-electron diffusion.^[20]

Supercapacitor Measurements

Three-Electrode Assembly

In Figure 5(A–C), the CV curves display the various scan speeds within the potential range between 0–0.46 V of NiCoFe LDH, g-C₃N₄, and the NiCoFe LDH/g-C₃N₄ composite. Figure 5(A–C) illustrates that all curves exhibit non-rectangular shapes with distinct redox peaks, distinguishing them from pseudocapacitive and EDLC materials (i.e., battery-type electrode materials).^[17c] The electrochemical characteristics of the various electrodes may be compared using the integral area of the CV curve.

The following is the order of the area integrated from CV curves: NiCoFe LDH/g-C₃N₄ > g-C₃N₄ > NiCoFe LDH (Figure S3). The NiCoFe LDH/g-C₃N₄ exhibits the highest integral area and redox peak intensity on the CV curve, suggesting a significantly improved specific capacity. Further, the effect of NiCoFe LDH/g-C₃N₄ composite composition on the performance of SC was performed by varying the amount of g-C₃N₄ to NiCoFe LDH. Figure S4(A) shows the CV curves of NiCoFe LDH/g-C₃N₄ (1:1 ratio), NiCoFe LDH/g-C₃N₄ (2:1 ratio), and NiCoFe LDH/g-C₃N₄ (1:2 ratio) composite at 5 mVs⁻¹. Figure S4(B) shows the NiCoFe

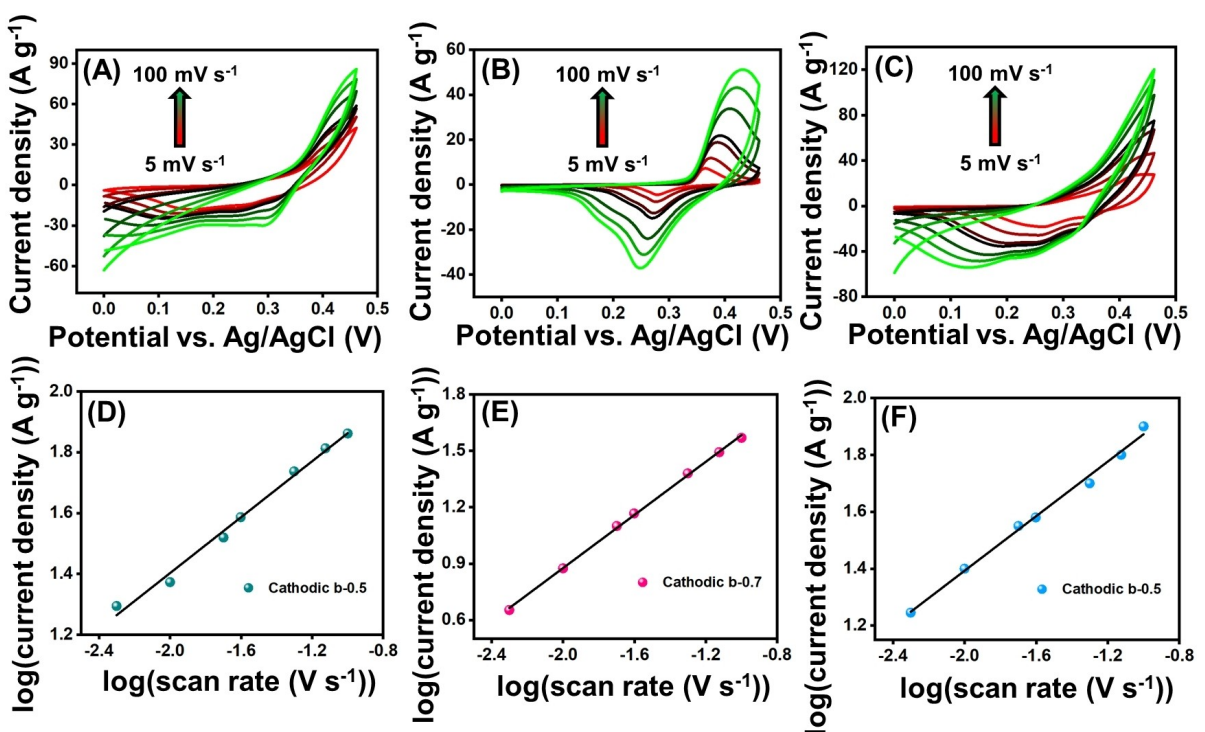


Figure 5. (A–C) CV curves obtained for NiCoFe LDH, g-C₃N₄ and NiCoFe LDH/g-C₃N₄ composite, respectively, at different scan rates (D–F) logarithmic plots of NiCoFe LDH, g-C₃N₄ and NiCoFe LDH/g-C₃N₄ composite, respectively.

LDH/g-C₃N₄ composite with a 1:1 ratio possesses a larger integral area than the composite with a 2:1 and 1:2 ratio of NiCoFe LDH/g-C₃N₄. An optimal 1:1 ratio promotes efficient interaction between NiCoFe LDH and g-C₃N₄, enhancing charge transfer pathways. The CV curves of the electrodes demonstrate the shift in redox peak location towards both ends of potential due to electrode polarization.^[17c,d]

The CV curves demonstrate the diffusive and surface-controlled behavior of the fabricated electrodes, representing a faradaic process. Moreover, the power law equation (eqn. (6 & 7) illustrates the ways in which charges accumulate in electroactive materials.^[17d,27] By taking the log of both sides of the Equation (6), where, a and b are the constants,

$$i = av^b \quad (6)$$

$$\log i = b \log v + \log a \quad (7)$$

When the slope b equals one, surface control governs the charge storage mechanism in this equation. In another example, the diffusion control process occurs when the slope b equals 0.5.^[27] In Figure 5(D–F), the b value obtained from the cathode peak is 0.5, 0.7, and 0.5 for the NiCoFe LDH, g-C₃N₄, and NiCoFe LDH/g-C₃N₄ composite. The b values indicate g-C₃N₄ shows both diffusion control and surface-controlled processes, while NiCoFe LDH and NiCoFe LDH/g-C₃N₄ composite show the diffusion-controlled process during the charge storage mechanism.

Equations (8) and (9) were used to divide the current response $i(v)$ into two parts: the diffusion-controlled process ($k_2v^{1/2}$) and the surface-controlled process (k_1v) to estimate the charge storage contribution accurately.

$$i(v) = k_1v + k_2v^{1/2} \quad (8)$$

$$\frac{i(v)}{v^{1/2}} = k_1 + k_2v^{1/2} \quad (9)$$

Figure 6(A–C) depicts the surface and diffusion-controlled processes of NiCoFe LDH, g-C₃N₄, and NiCoFe LDH/g-C₃N₄ electrodes at 10 mVs⁻¹. The NiCoFe LDH, g-C₃N₄, and NiCoFe LDH/g-C₃N₄ composite shows the diffusion-controlled process at about 86.1%, 71.8%, and 87.5%, respectively, and the surface-controlled process at about 13.9%, 28.2%, and 12.5%, respectively. Figure 6(D–F) shows the charge storage contribution of NiCoFe LDH, g-C₃N₄, and NiCoFe LDH/g-C₃N₄ electrodes at various scan rates, respectively. It is observed that the surface-controlled processes increased with increasing scan rate; as the scan rates increased, the surface-controlled mechanism is found to be increased. On the other hand, the diffusion-controlled mechanism is found to be reduced.

Figure 7A compares the GCD curves of NiCoFe LDH, g-C₃N₄, and NiCoFe LDH/g-C₃N₄ composite electrodes produced at a current density of 1 Ag⁻¹. Furthermore, Figure 7B and Figure S5(A and B) show the GCD analysis of the NiCoFe LDH/g-C₃N₄ composite, NiCoFe LDH, and g-C₃N₄ electrodes at various current densities. The GCD curves of all produced electrodes show nonlinear triangular patterns. A voltage plateau at the starting position discharging section indicates that the electrodes follow the faradaic nature of the battery-type mechanism, which is compatible with the behavior exhibited on CV curves. Based on the observation from Figure 7A, it can be concluded that the discharge duration of the NiCoFe LDH/g-C₃N₄ composite electrode is longer compared to the NiCoFe LDH and g-C₃N₄.

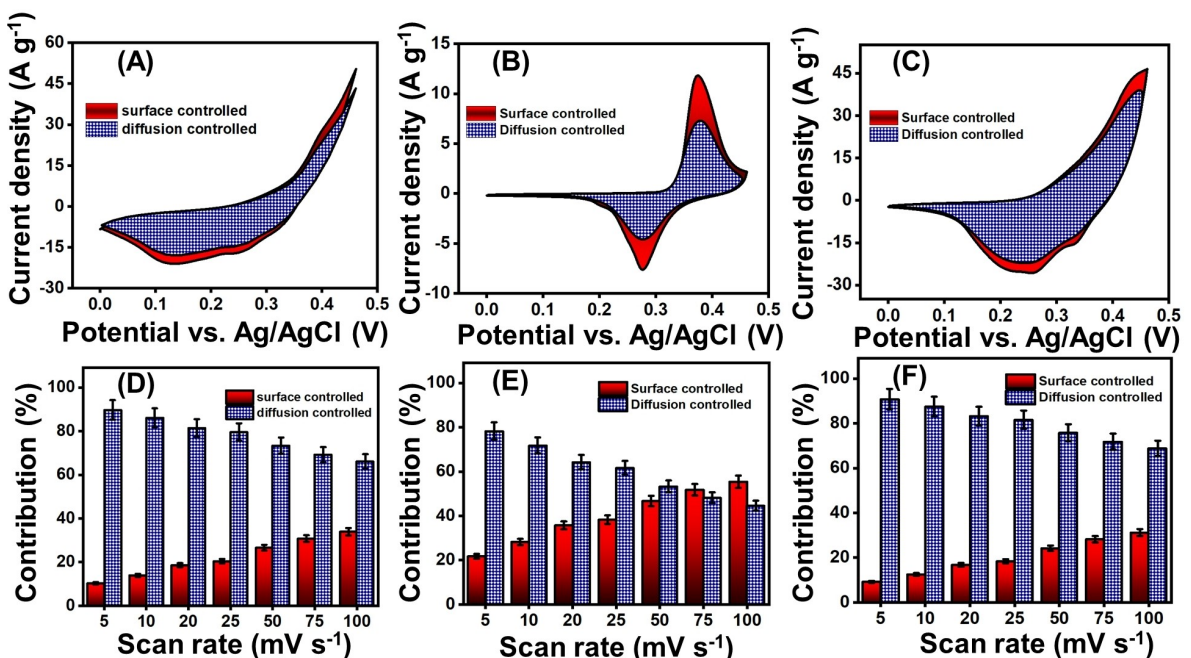


Figure 6. (A–C) Surface and diffusion-controlled contribution of NiCoFe LDH, g-C₃N₄ and NiCoFe LDH/g-C₃N₄ electrode, respectively at 10 mV s⁻¹ (D–F) Overall contributions NiCoFe LDH, g-C₃N₄ and NiCoFe LDH/g-C₃N₄ electrodes at various scan rates

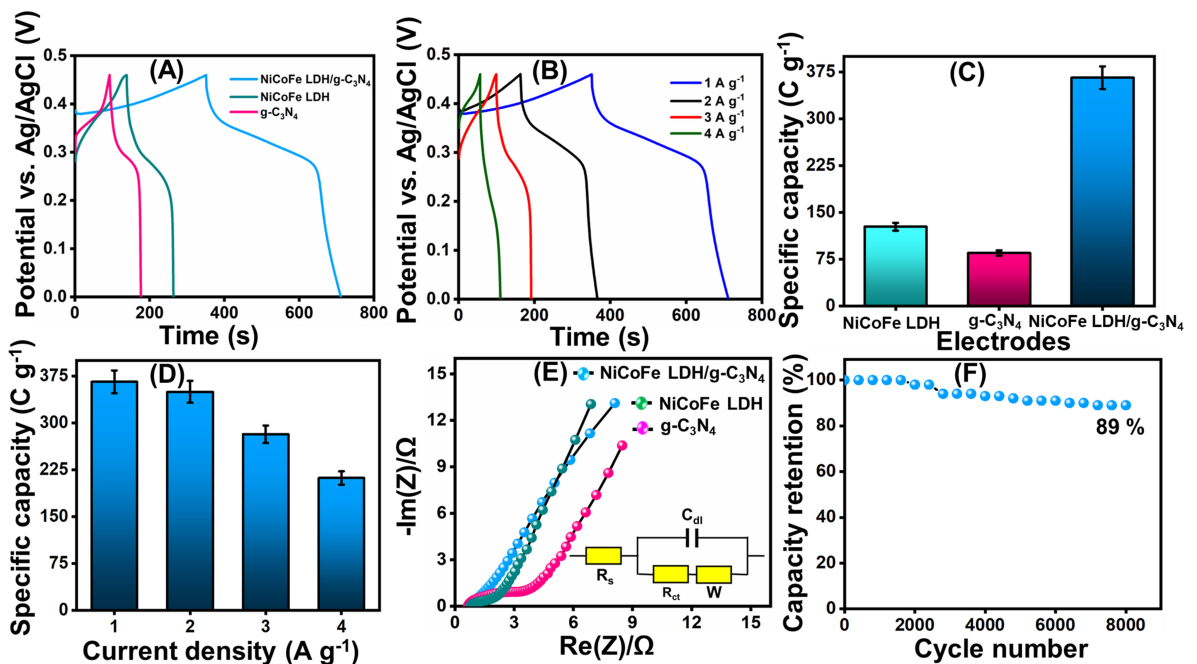


Figure 7. (A) GCD curve of NiCoFe LDH, g-C₃N₄ and NiCoFe LDH/g-C₃N₄ composite electrode at a current density of 1 A g⁻¹ (B) GCD curves of NiCoFe LDH/g-C₃N₄ composite at various current densities (C) comparison of the specific capacity of the different electrodes (D) bar diagram of current density vs. specific capacity (E) EIS analysis of NiCoFe LDH, g-C₃N₄ and NiCoFe LDH/g-C₃N₄ composite (F) cyclic stability analysis

C₃N₄ electrodes. Thus, it can be inferred that the NiCoFe LDH/g-C₃N₄ composite electrode exhibits the highest discharge-specific capacity compared to all other electrodes.^[28]

The specific capacity values of NiCoFe LDH, g-C₃N₄, and NiCoFe LDH/g-C₃N₄ composite electrodes were determined to be 127 C g⁻¹, 85 C g⁻¹, and 366 C g⁻¹, respectively, with an applied current density of 1 A g⁻¹ (Figure 7C). The NiCoFe-LDH/g-C₃N₄ composite has the highest specific capacity due to the combined effect of several Faraday redox processes in the ternary LDH composite. The distinctive nanoscale architecture of the NiCoFe LDH/g-C₃N₄ composite provides a large number of accessible active sites and a large number of pores, which promote a significant interaction between the electrode and the electrolyte. The combination of NiCoFe-LDH and g-C₃N₄ in

the composites results in a synergistic effect that enhances conductivity, catalytic activity, and stability of the materials. As a result, the charge storage capacity is increased for the NiCoFe-LDH/g-C₃N₄ composite.^[15b]

Furthermore, it is observed that the C_{sp} of the electrode is found to be decreased as the current density increases (Figure 7D). At high current densities, electrolyte ions have a restricted ability to diffuse through the electrode/electrolyte interface rapidly, and their interaction with the electrode surface is sluggish. In addition, the capacity performances of the NiCoFe-LDH/g-C₃N₄ composite electrode were compared to those of other LDH and g-C₃N₄-based supercapacitor materials shown in Table 1, which proved improved supercapacitor behavior of the NiCoFe-LDH/g-C₃N₄ composite than the other

Table 1. Electrochemical performance of different electroactive materials containing NiCoFe-LDH and g-C₃N₄ for supercapacitors.

Electrode materials	Specific capacitance F g ⁻¹ (A g ⁻¹)	Capacitance retention	Ref.
Mg/Fe-LDH	147 (3)	92.12 % (1000 cycles)	[30]
LDH/PANI	717 (2)	84.7 % (1000 cycles)	[31]
Ni(OH) ₂ /rGO	768 (2)	90 % (2000 cycles)	[32]
CoAl-LDH/PEDOT	672 (1)	92.5 % (5000 cycles)	[33]
NiCoFe-LDH	409 (2)	90.9 % (1000 cycles)	[31]
GCN/NCS-1	403.6 (0.1)	85.5 % (5000 cycles)	[34]
NiCo ₂ S ₄ NSs/P-g-C ₃ N ₄	277 (1)	99 % (5000 cycles)	[35]
NiCoFe LDH/g-C ₃ N ₄	795 (366 C g ⁻¹) at 1 A g ⁻¹	89 % (8000 cycles)	This work

This work reports a facile synthesis of NiCoFe LDH/g-C₃N₄ composite as the positive electrode material for the hybrid supercapacitor application. The NiCoFe LDH/g-C₃N₄//AC

reported works.^[30–35] This might be attributed to the perfect synergistic effect between NiCoFe LDH and g-C₃N₄, and the significant surface area of the composite which facilitates the electrochemical behavior of the composite. The results indicate that NiCoFe-LDH/g-C₃N₄ composite had a notable specific capacity, making it an excellent candidate for use as an electrode in supercapacitors.^[29]

The electrochemical performance of the electrodes that have been created is also confirmed through the use of EIS technology. The Nyquist plots of three electrode materials are shown in Figure 7E, which shows an angled semicircle with a half-line sloped at both high and low frequencies. The semicircle arises from the capacitive characteristics of the material due to its ability to migrate the charges. Charge transfer resistance (R_{ct}) and solution resistance (R_s) contribute to electrochemical resistance.^[36] The R_{ct} values for the electrodes are determined to be 1.51 Ω, 2.97 Ω, and 0.75 Ω for NiCoFe LDH, g-C₃N₄, and NiCoFe-LDH/g-C₃N₄ electrodes, respectively. R_s refers to the point where the curve intersects with the real axis, and the values are obtained to be 0.63 Ω, 0.67 Ω, and 0.59 Ω for the NiCoFe LDH, g-C₃N₄, and NiCoFe-LDH/g-C₃N₄ electrodes, respectively. The NiCoFe-LDH/g-C₃N₄ electrodes exhibited much lower charge-transfer resistance (R_{ct}) than the NiCoFe LDH and g-C₃N₄. This suggests the rapid charge transfer and transport process occurred in the NiCoFe-LDH/g-C₃N₄ electrodes. Therefore, the NiCoFe-LDH/g-C₃N₄ composite demonstrated higher electrochemical performance due to improved electron and ion transportation pathways.^[20,37]

Usually, the key need for the utilization of supercapacitors is the capacity of electrode materials to maintain stability over extended periods of use. As illustrated in Figure 7F, the cyclic performance of NiCoFe LDH/g-C₃N₄ composite is carried out by 8000 GCD cycles at 6 A g⁻¹. The capacitance retention of the electrode increases slightly during the first 1000 cycles. This can be attributed to electrode activation during the charging and discharging process, as well as the slow infiltration of the

electrolyte solution into the active material. As a result, more number of active sites grows in the reactions. After 6000 GCD cycles, the capacity retention rate decreases due to degradation of the structure electrode material, induced by frequent charging and discharging. This degradation results in a drop-in activity. After 8000 GCD cycles, the capacity retention maintains at 89%. The potential factors contributing to the exceptional cycling performance of the NiCoFe LDH/g-C₃N₄ composite electrode material might be due to the combination of NiCoFe-LDH and g-C₃N₄ has a synergistic impact, enhancing the function of redox reactions.^[14,38]

Two Electrode Measurement- NiCoFe LDH/g-C₃N₄//AC HSC

In order to explore potential uses of NiCoFe LDH/g-C₃N₄ composite, a hybrid supercapacitor (HSC) is constructed according to the diagram in Figure 8A. In this setup, NiCoFe LDH/g-C₃N₄ is utilized as the positive (battery-type) and AC serves as the negative (capacitive-type) electrodes. Figure 8B displays CV of the AC and NiCoFe LDH/g-C₃N₄ electrodes at a scan rate of 50 mV s⁻¹. In the range of -1 to 0 V, the AC electrode displays a distinctive CV curve that is rectangular in shape and typical of an electric double-layer capacitor (EDLC). The NiCoFe LDH/g-C₃N₄ electrode exhibits battery-like behavior within the voltage window of 0–0.46 V. Thus, it can be theoretically inferred that the NiCoFe LDH/g-C₃N₄//AC HSC equipment has a maximum voltage range of 0–1.46 V. To confirm the perfect voltage range, the CV analysis was performed with different voltage window (0 V to 1.8 V) at 50 mV s⁻¹, as shown in Figure 8C. After 0–1.6 V, the polarization of electrode materials occurs and it becomes higher as the potential climbs to 0–1.8 V. To ensure device safety, the optimal voltage range was set to 0–1.6 V.

Figure 8D shows the CV curves of the HSC at different sweep speeds, demonstrating that the CV curves lack distinguishable redox peaks, implying that the device exhibits

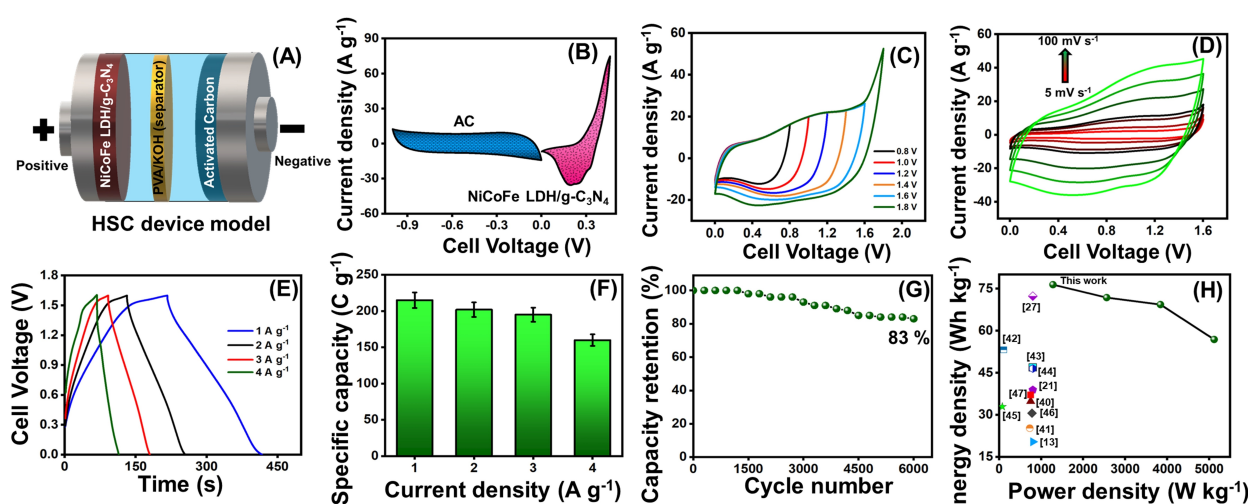


Figure 8. (A) Schematic representation of NiCoFe LDH/g-C₃N₄//AC HSC (B) CV curves of NiCoFe LDH/g-C₃N₄ (positive) and AC (negative) electrode at 50 mV s⁻¹ (C) CV curves of NiCoFe LDH/g-C₃N₄//AC HSC at different potential windows (D) CV curves of as-constructed HSC at different scan rates (E) GCD curves of NiCoFe LDH/g-C₃N₄//AC HSC at different current densities (F) bar diagram of current density vs. specific capacity (G) cyclic stability (H) Ragone plot

battery-like behavior.^[17c] The CV curve has a uniform shape across different scan rates, providing evidence of the reversibility of the fabricated device. The GCD curves of the as-fabricated HSC device at various current densities are displayed in Figure 8E. The nearly identically shaped GCD curves at all current densities indicate that the HSC device demonstrated exceptional coulombic efficiency. Furthermore, it was determined that the NiCoFe LDH/g-C₃N₄//AC had an estimated specific capacity of 215 Cg⁻¹ at 1 Ag⁻¹. The obtained C_{sp} at different current densities is shown in Figure 8F, where a negative correlation could be caused by the time-limiting mechanism.^[17d]

Furthermore, the cycling performance of the NiCoFe LDH/g-C₃N₄//AC hybrid supercapacitor was tested using 6000 GCD cycles at 6 Ag⁻¹, as shown in Figure 8G. After undergoing 6000 GCD cycles, the HSC device retains 83% of its initial capacitance, suggesting excellent durability of the device. The as-fabricated NiCoFe LDH/g-C₃N₄//AC HSC exhibits an impressive energy density of 76.44 Wh kg⁻¹, corresponding to a power density of 1279.9 W kg⁻¹ at 1 Ag⁻¹. The Ragone plot of the NiCoFe LDH/g-C₃N₄//AC HSC with a comparison of other HSC devices is shown in Figure 8H.^[39] The obtained energy density outperforms other comparable studies, such as the CNTs/NiCo LDH//AC (38.9 Wh kg⁻¹ at 800 W kg⁻¹),^[21] NiCoP@NiCoP//AC (34.8 Wh kg⁻¹ at 750 W kg⁻¹),^[40] NiCo₂O₄//rGO (25.24 Wh kg⁻¹ at 727 W kg⁻¹),^[41] Co₃O₄@LDH//carbon nanosheets (53.2 Wh kg⁻¹ at 105 W kg⁻¹),^[42] PPy-rGO//rGO (46.9 Wh kg⁻¹ at 800 W kg⁻¹),^[43] Ni-Co-S/CNT//CNT (46.5 Wh kg⁻¹ at 800 W kg⁻¹),^[44] CoNi LDH nanospheres//AC (32.9 Wh kg⁻¹ at 74.3 W kg⁻¹),^[45] CoNi LDH nanoflakes//AC (20.38 Wh kg⁻¹ at 800 W kg⁻¹),^[13] NiV LDH//AC (30.6 Wh kg⁻¹ at 780 W kg⁻¹),^[46] CoNi LDH nanoflower//AC (37.1 Wh kg⁻¹ at 748 W kg⁻¹),^[47] NiCoFe_{0.75}-LDH-Se//NiCo-O-Se//AC (72.3 Wh kg⁻¹ at 800 W kg⁻¹).^[27] Because of the synergistic effect of NiCoFe LDH and g-C₃N₄, which gives the composite material extraordinary electrical conductivity, NiCoFe LDH/g-C₃N₄//AC HSC exhibits remarkable supercapacitive qualities. Numerous investigations have demonstrated that the presence of Ni element can give a significant increase in specific capacity. High electrical conductivity is another feature of the Co element, whereas the Fe element increases the number of active sites and stabilizes the electronic structure. Effective ion and electron diffusion is made possible by the large surface area produced by the arrangement of flexible nanosheets in a porous structure. The 2D structure combines the benefits of a layered structure with a porous morphology, resulting in improved space utilization, increased availability of redox active sites, and enhanced stability of the NiCoFe LDH/g-C₃N₄ electrode.^[17c] In summary, NiCoFe LDH/g-C₃N₄ electrodes have exhibited exceptional performance as electrode materials, offering an innovative perspective for the future development of hybrid energy storage devices.

Conclusions

In this work, a simple hydrothermal method was used to prepare the NiCoFe LDH/g-C₃N₄ composite. Different spectral

and analytical tools demonstrated the formation of the NiCoFe LDH/g-C₃N₄ composite. The SEM and TEM images illustrate the growth of a flower-like structure through the arrangement of nanosheets. The NiCoFe LDH/g-C₃N₄ composite electrode exhibits battery-like characteristics in supercapacitor measurements with a specific capacity of 366 Cg⁻¹ at a current density of 1 Ag⁻¹. The EIS investigation verified that the NiCoFe LDH/g-C₃N₄ composite exhibited lower resistance than the individual NiCoFe LDH and g-C₃N₄ electrodes. Furthermore, the NiCoFe LDH/g-C₃N₄ composite electrode exhibits an impressive 89% capacity retention even after 8000 GCD cycles. In addition, a hybrid supercapacitor was constructed by utilizing a combination of NiCoFe LDH/g-C₃N₄ as the positive electrode material and AC as the negative electrode material. The HSC device has shown a specific capacity of 215 Cg⁻¹, a remarkable energy density of 76.44 Wh kg⁻¹, and a power density of 1279.9 W kg⁻¹. The exceptional electrochemical performance was mainly due to the synergistic interaction between NiCoFe LDH and g-C₃N₄, as well as the unique nanoarchitecture of the NiCoFe LDH/g-C₃N₄ composite. These findings demonstrate that NiCoFe LDH/g-C₃N₄ possesses significant promise as an active electrode material in forthcoming supercapacitors.

Acknowledgements

The authors express gratitude to the Ministry of Science and Technology and the National Taipei University of Technology in Taiwan for providing research funds for the project (Special Research Project-MOST-108-2221-E-027-063).

Conflict of Interests

The authors declare no conflict of interest.

Data Availability Statement

Research data are not shared.

Keywords: NiCoFe LDH • g-C₃N₄ • Activated carbon • Specific capacity • Hybrid supercapacitor

- [1] a) F. Liu, Y. Chen, Y. Liu, J. Bao, M. Han, Z. Dai, *Nanoscale* **2019**, *11*, 9896–9905; b) Y. Fu, H. Wu, S. Ye, X. Cai, X. Yu, S. Hou, H. Kafafy, D. Zou, *Energy Environ. Sci.* **2013**, *6*, 805–812.
- [2] H.-J. Choi, S.-M. Jung, J.-M. Seo, D. W. Chang, L. Dai, J.-B. Baek, *Nano Energy* **2012**, *1*, 534–551.
- [3] a) F. Liao, G. Yang, Q. Cheng, L. Mao, X. Zhao, L. J. Chen, *Electrochim. Acta* **2022**, *428*, 140939; b) Y. Ai, C. Yang, Z. Yin, T. Wang, T. Gai, J. Feng, K. Li, W. Zhang, Y. Li, F. Wang, *J. Am. Chem. Soc.* **2024**, *146*, 15496–15505; c) T. Shu, X. Yang, Z. Huang, M. Qiao, J. Ning, K. Li, Y. Zhang, L. Li, X. Liu, K. X. Yao, *J. Mater. Chem. A* **2024**, *12*, 4666–4677; d) K. Li, Z. Guo, Q. Sun, X. Dai, Y. Li, K. Yao, X. Liu, Z. Bao, J. Rao, Y. Zhang, *Chem. Eng. J.* **2023**, *454*, 140223; e) K. Li, C. Yin, X. Dai, J. Zhang, S. Yi, J. Rao, Y. Zhang, *J. Energy Storage* **2022**, *55*, 105722; f) C. Zhang, K. Li, T. Sun, X. Liu, X. Dai, Q. Zhou, D. Wang, X. Zhang, J. Ding, X. Huang, *ACS Appl. Nano Mater.* **2024**, *7*, 3001–3011.

- [4] D. Chen, Q. Wang, R. Wang, G. Shen, *J. Mater. Chem. A* **2015**, *3*, 10158–10173.
- [5] a) Z. Gao, C. Bumgardner, N. Song, Y. Zhang, J. Li, X. Li, *Nat. Commun.* **2016**, *7*, 11586; b) J. Cao, X. Li, Y. Wang, F. C. Walsh, J.-H. Ouyang, D. Jia, Y. Zhou, *J. Power Sources* **2015**, *293*, 657–674; c) Q. Kang, L. Ye, B. Xu, C. An, S. J. Stuard, S. Zhang, H. Yao, H. Ade, J. Hou, *Joule* **2019**, *3*, 227–239.
- [6] P. Nakhanivej, X. Yu, S. K. Park, S. Kim, J.-Y. Hong, H. J. Kim, W. Lee, J. Y. Hwang, J. E. Yang, C. Wolverton, *Nat. Mater.* **2019**, *18*, 156–162.
- [7] Q. Wang, Y. Luo, R. Hou, S. Zaman, K. Qi, H. Liu, H. S. Park, B. Y. Xia, *Adv. Mater.* **2019**, *31*, 1905744.
- [8] a) L. Mao, X. Zhao, Y. Li, L. Chen, *J. Colloid Interface Sci.* **2022**, *624*, 482–493; b) J. Zhao, J. Chen, S. Xu, M. Shao, D. Yan, M. Wei, D. G. Evans, X. Duan, *J. Mater. Chem. A* **2013**, *1*, 8836–8843.
- [9] A. Mahmood, Q. Yu, Y. Luo, Z. Zhang, C. Zhang, L. Qiu, B. Liu, *Nanoscale* **2020**, *12*, 10751–10759.
- [10] Y. Li, B. Huang, X. Zhao, Z. Luo, S. Liang, H. Qin, L. Chen, *J. Power Sources* **2022**, *527*, 231149.
- [11] a) J. B. Gerken, J. G. McAlpin, J. Y. Chen, M. L. Rigsby, W. H. Casey, R. D. Britt, S. S. Stahl, *J. Am. Chem. Soc.* **2011**, *133*, 14431–14442; b) Q. Wang, X. Ma, P. Wu, B. Li, L. Zhang, J. Shi, *Nano Energy* **2021**, *89*, 106326.
- [12] a) M. Guo, L. Ye, L. Zhao, *J. Alloys Compd.* **2021**, *850*, 156787; b) J. Wang, Q. Ding, C. Bai, F. Wang, S. Sun, Y. Xu, H. Li, *Nanomaterials* **2021**, *11*, 2155.
- [13] B. Huang, W. Wang, T. Pu, J. Li, J. Zhu, C. Zhao, L. Xie, L. Chen, *J. Colloid Interface Sci.* **2018**, *532*, 630–640.
- [14] M. Pourshahmir, S. Ghasemi, S. R. Hosseini, *Int. J. Hydrogen Energy* **2023**, *48*, 8127–8143.
- [15] a) C. Chen, X. Deng, Y. Deng, L. An, Y. Deng, Y. Zheng, D. Dang, X. Yang, *Int. J. Hydrogen Energy* **2022**, *47*, 14896–14905; b) Z. Sheng, X. Lin, H. Gao, L. Huang, Y. Zhang, Y. Zhao, H. Wei, C. Wang, D. Xu, Y. Wang, *Int. J. Hydrogen Energy* **2022**, *47*, 29195–29206.
- [16] a) Y. Liu, C. Xiang, H. Chu, S. Qiu, J. McLeod, Z. She, F. Xu, L. Sun, Y. Zou, *J. Mater. Sci. Technol.* **2020**, *37*, 135–142; b) X. Hong, K. Hui, Z. Zeng, K. Hui, L. Zhang, M. Mo, M. Li, *Electrochim. Acta* **2014**, *130*, 464–469.
- [17] a) Q. Xie, X. Huang, Y. Zhang, S. Wu, P. Zhao, *Appl. Surf. Sci.* **2018**, *443*, 412–420; b) S. Fan, L. Wei, X. Liu, W. Ma, C. Lou, J. Wang, Y. Zhang, *Int. J. Hydrogen Energy* **2021**, *46*, 39969–39982; c) E. Elanthamilan, S.-F. Wang, *J. Energy Storage* **2024**, *99*, 113262; d) A. Sathiyan, E. Elanthamilan, S.-F. Wang, S. Dhineshkumar, J. P. Merlin, *New J. Chem.* **2024**, *48*, 3080–3088.
- [18] a) Y. Feng, X. Jiang, L. Tang, D. Lin, Y. Huo, F. Xie, Q. Zheng, *Catal. Lett.* **2022**, *152*, 1719–1728; b) D. Zhou, Z. Cai, Y. Jia, X. Xiong, Q. Xie, S. Wang, Y. Zhang, W. Liu, H. Duan, X. Sun, *Nanoscale Horiz.* **2018**, *3*, 532–537.
- [19] a) H. Qiu, Q. Ma, X. Sun, X. Han, G. Jia, Y. Zhang, W. He, *J. Alloys Compd.* **2022**, *896*, 163023; b) S. Liu, S. C. Lee, U. Patil, I. Shackery, S. Kang, K. Zhang, J. H. Park, K. Y. Chung, S. C. Jun, *J. Mater. Chem. A* **2017**, *5*, 1043–1049.
- [20] E. Elanthamilan, M. Sasikumar, S.-F. Wang, *Appl. Surf. Sci. Adv.* **2023**, *18*, 100516.
- [21] N. Zhao, Y. Feng, H. Zhao, H. Fan, S. Tian, B. Hu, *J. Alloys Compd.* **2022**, *901*, 163566.
- [22] a) D. Wadkar, K. JadHAV, S. Jituri, S. Mujawar, *J. Mater. Sci. Mater. Electron.* **2024**, *35*, 1037; b) M. Praveen Kumar, M. Sasikumar, A. Arulraj, V. Rajasudha, G. Murugadoss, M. R. Kumar, S. Gouse Peera, R. V. Mangalaraja, *Catalysts* **2022**, *12*, 1470; c) X. Cai, X. Shen, L. Ma, Z. Ji, C. Xu, A. Yuan, *Chem. Eng. J.* **2015**, *268*, 251–259.
- [23] a) N. Shabana, A. M. Arjun, K. Rajendran, S. Pathan, P. A. Rasheed, *Anal. Methods* **2023**, *15*, 587–595; b) C. Fan, J. Miao, G. Xu, J. Liu, J. Lv, Y. Wu, *RSC Adv.* **2017**, *7*, 37185–37193.
- [24] J. Shang, Y. Zhang, Q. Zhang, Y. Li, F. Deng, R. Gao, J. Wang, *J. Alloys Compd.* **2022**, *925*, 166668.
- [25] Y. Zhang, J. Shang, Q. Zhang, Y. Li, F. Deng, J. Wang, R. Gao, *J. Alloys Compd.* **2024**, *970*, 172521.
- [26] H. He, S. Lv, Y. Kang, J. Yi, Y. Zhang, Y. Cong, *J. Electroanal. Chem.* **2022**, *919*, 116540.
- [27] R. Luo, Q. Yang, Y. Liu, L. Sun, C. Wang, M. Chen, W. Shi, *Chem. Eng. Sci.* **2024**, *283*, 119438.
- [28] a) A. E. Elkholly, F. E.-T. Heakal, N. K. Allam, *Electrochim. Acta* **2019**, *296*, 59–68; b) Y. Li, Z. Luo, S. Liang, H. Qin, X. Zhao, L. Chen, H. Wang, S. Chen, *J. Mater. Sci. Technol.* **2021**, *89*, 199–208.
- [29] R. Yang, J. Yesuraj, K. Kim, *J. Power Sources* **2023**, *586*, 233642.
- [30] J. Han, H.-Y. Zeng, X. Cao, C.-R. Chen, *J. Mater. Sci. Mater. Electron.* **2017**, *28*, 2754–2762.
- [31] L. Liu, X. Hu, H.-Y. Zeng, M.-Y. Yi, S.-G. Shen, S. Xu, X. Cao, J.-Z. Du, *J. Mater. Sci. Technol.* **2019**, *35*, 1691–1699.
- [32] P. Shen, H. Zhang, S. Zhang, L. Fei, *Appl. Surf. Sci.* **2018**, *460*, 65–73.
- [33] J. Han, Y. Dou, J. Zhao, M. Wei, D. G. Evans, X. Duan, *Small* **2013**, *9*, 98–106.
- [34] J. Zhu, L. Kong, X. Shen, H. Zhou, G. Zhu, Z. Ji, K. Xu, S. A. Shah, *Dalton Trans.* **2018**, *47*, 9724–9732.
- [35] Z. Li, L. Wu, L. Wang, A. Gu, Q. Zhou, *Electrochim. Acta* **2017**, *231*, 617–625.
- [36] E. Elanthamilan, S. Rajkumar, J. P. Merlin, D. S. Jona, K. Monisha, B. C. Meena, *Electrochim. Acta* **2020**, *359*, 136953.
- [37] J. Tian, A. Zhang, R. Liu, W. Huang, Z. Yuan, R. Zheng, D. Wei, J. Liu, *J. Colloid Interface Sci.* **2020**, *579*, 607–618.
- [38] T. Shahanas, J. Yesuraj, G. Harichandran, B. Muthuraaman, K. Kim, *J. Alloys Compd.* **2023**, *933*, 167645.
- [39] R. Hou, G. S. Gund, K. Qi, P. Nakhanivej, H. Liu, F. Li, B. Y. Xia, H. S. Park, *Energy Storage Mater.* **2019**, *19*, 212–241.
- [40] Y. Zhu, Q. Zong, Q. Zhang, H. Yang, Q. Wang, H. Wang, *Electrochim. Acta* **2019**, *299*, 441–450.
- [41] K. H. Oh, G. S. Gund, H. S. Park, *J. Mater. Chem. A* **2018**, *6*, 22106–22114.
- [42] L. Zhang, K. Hui, K. Hui, S. W. Or, *Dalton Trans.* **2019**, *48*, 150–157.
- [43] X. Zhang, J. Zhang, Y. Chen, K. Cheng, J. Yan, K. Zhu, K. Ye, G. Wang, L. Zhou, D. Cao, *J. Colloid Interface Sci.* **2019**, *536*, 291–299.
- [44] T. Peng, H. Yi, P. Sun, Y. Jing, R. Wang, H. Wang, X. Wang, *J. Mater. Chem. A* **2016**, *4*, 8888–8897.
- [45] Z. Xiao, Y. Mei, S. Yuan, H. Mei, B. Xu, Y. Bao, L. Fan, W. Kang, F. Dai, R. Wang, *ACS Nano* **2019**, *13*, 7024–7030.
- [46] A. Tyagi, M. C. Joshi, A. Shah, V. K. Thakur, R. K. Gupta, *ACS Omega* **2019**, *4*, 3257–3267.
- [47] E. Bao, X. Ren, Y. Wang, Z. Zhang, C. Luo, X. Liu, C. Xu, H. Chen, *J. Energy Storage* **2024**, *82*, 110535.

Manuscript received: November 29, 2024

Revised manuscript received: January 20, 2025

Accepted manuscript online: January 27, 2025

Version of record online: February 9, 2025